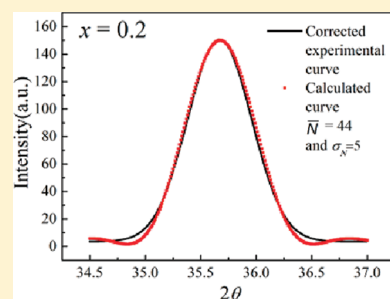


Magnetic Behavior of Zn-Doped Fe_3O_4 Nanoparticles Estimated in Terms of Crystal Domain Size

Jun Liu, Yuezheng Bin, and Masaru Matsuo*

Department of Polymer Science and Material, Dalian University of Technology, Dalian 116024, People's Republic of China

ABSTRACT: A series of zinc (Zn) doped Fe_3O_4 nanoparticles with different Zn concentrations represented as $\text{Zn}_x\text{Fe}_{3-x}\text{O}_4$ ($0 < x \leq 1$) were synthesized by the chemical coprecipitated technique mainly in the presence of sodium dodecyl benzene sulfonate (SDBS) as one of the surface modifiers. The prepared zinc-doped Fe_3O_4 nanoparticles were characterized by a vibrating sample magnetometer (VSM), wide-angle X-ray diffraction (WAXD), and transmission electron microscopy (TEM). The VSM measurements showed that magnetization vs applied magnetic field for zinc-doped particles showed an increasing curve with very small hysteresis and that the saturation magnetization (M_s) of $\text{Zn}_x\text{Fe}_{3-x}\text{O}_4$ reached a maximum 80.93 emu/g at $x = 0.2$. The experimental result exhibited that $\text{Zn}_{0.2}\text{Fe}_{2.8}\text{O}_4$ nanoparticles coated with different surface modifiers give good dispersivity and outstanding stability in the organic dispersed phase compared with noncoated particles. The value of M_s decreased with further increase in x beyond 0.2. Such decreasing behavior of the magnetization was elucidated on the basis of two factors. One was the comparison between experimental and calculated curves of the average magnetic moment of paramagnetism associated with superexchange interactions among magnetic ions in tetrahedral space (A-site) and octahedral space (B-site) in a crystal unit with face-centered cubic inverse-spinel structure. The second was x -dependence on the WAXD curve profile calculated based on the modified Laue function for a diffraction peak from the (311) plane. The observed and calculated WAXD intensity curves revealed that the a -axis became longer and the corresponding crystal size became smaller with increasing x up to 0.4. In contrast, further increase beyond 0.4 provided the inverse relationships. The a -axis became shorter, and the crystal size became bigger. They were close to those of Fe_3O_4 at $x = 1$, indicating that $x = 0.4$ is the zinc doping limit to form a zinc-doped Fe_3O_4 crystal structure.



INTRODUCTION

The Fe_3O_4 nanoparticle is one of the most important nanostructured magnetic materials and has attracted increasing attention over the past decade owing to its unique electrical and magnetic properties such as superparamagnetism.¹ One of the remarkable advantages for the magnetic particles is the generation of superparamagnetism, when the particle size of Fe_3O_4 becomes smaller than the critical diameter (D_c). Different from the bulk counterparts, the magnetic materials are no longer ferromagnetic but present superparamagnetism with negligibly small hysteresis, in which the residual magnetism (M_r) and the coercivity (H_c) are both close to zero.^{2–4} Despite removal of an external magnetic field, the excellent magnetic properties of superparamagnetic particulates can be ensured since no residual magnetic force exists among the particles. A number of studies for the Fe_3O_4 nanoparticle with superparamagnetism have already made substantial progress in application of pigment,⁵ magnetic fluids,⁶ catalysts,⁷ microwave absorption materials,⁸ lithium ion batteries,⁹ magnetic resonance imaging (MRI),¹⁰ bioseparations,¹¹ drug delivery,¹² and other biomedical applications.¹³

However, these applications still have a number of constraints, such as low magnetization as well as poor dispersibility and stability in organic solvent and polymer matrix.^{14,15} Magnetic property is well-known to be sensitive to the crystal structure and domain size. As described in established papers, the ferromagnetic material, Fe_3O_4 particles, displays superparamagnetic behavior at room temperature when its magnetic particles become

smaller than the critical particle domain size which has been reported as 128 nm.^{4,15} The number of magnetic domains of Fe_3O_4 decreased dramatically along with the decreasing particle domain diameter to the nanometer grade and resulted in the decrease of saturation magnetization (M_s) due to spin coating and surface effects.^{16,17} Typically, the M_s value for Fe_3O_4 nanometer microparticles reported as about 50 emu/g^{2,16,18} is much lower than that of bulk ferroferric oxide (85–100 emu/g).^{13,19} Furthermore, magnetization can vary in a wide range by synthesis methods associated with impurity addition, disrupting the crystal structure of magnetic materials. These synthesis techniques include the high-energy ball milling method,²⁰ gas-phase method,²¹ coprecipitation method,²² two-phase method,²³ sol–gel method,²⁴ hydrothermal method,²⁵ carbothermal reduction method,²⁶ and so on.

The magnetization and dispersibility can be improved through metal element doping and surface modification, respectively. Following reports in the literature, a series of synthesized inverse-spinel ferrite materials are commonly recorded as MFe_2O_4 doping with various divalent metallic elements including Zn, Co, Ni, Ba, Cu, and Mn represented as M.^{27–31} Zn is one of the most commonly used elements to dope into Fe_3O_4 .^{32–36} Magnetism for Fe_3O_4 arises from the indirect interactions among the cations in inverse-spinel structure. The oxygen ions (O^{2-}) are

Received: August 1, 2011

Revised: November 29, 2011

Published: November 30, 2011

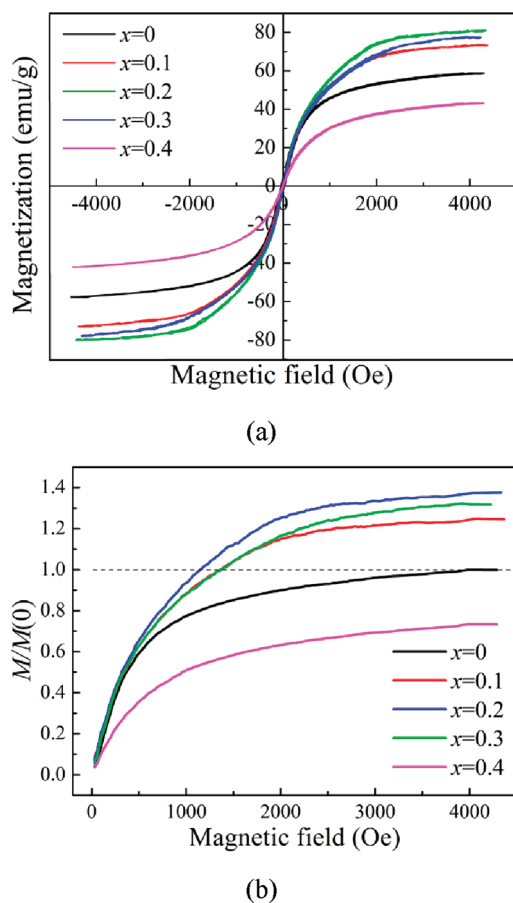


Figure 1. Field-dependent magnetization of $\text{Zn}_x\text{Fe}_{3-x}\text{O}_4$ with different Zn^{2+} contents at room temperature. (a) Original curves. (b) Curves normalized by $M(0)$ at 4400 Oe.

arranged in a staggered pattern forming face-centered cubic (FCC) lattice where there are two kinds of sublattices, namely, tetrahedral (A-site) and octahedral (B-site) interstitial sites.³⁷ The cations that occupy singly these interstitial positions interact with each other indirectly via oxygen anions, that is, superexchange interactions.^{18,38} The influence of metallic ions-dopant to magnetic materials operates as the alteration of superexchange interactions sensitive to the category and the location of metallic ions. Therewith, the magnetic properties of ferrite materials change along with superexchange interactions. At present, there are quite a lot of relevant reports on the synthesis of ferrite doping with metallic elements, but the mechanisms for superexchange interactions and magnetism have seldom been explained in depth in terms of quantitative analysis of WAXD intensity curves.

In an attempt to explore the relationship between magnetism and zinc doping, this paper deals with a series of zinc ferrite recorded as $\text{Zn}_x\text{Fe}_{3-x}\text{O}_4$ ($0 \leq x \leq 1$), x being the amount of Zn doped into Fe_3O_4 , prepared through the chemical coprecipitation method. The magnetization is discussed in relation to the stability of the resultant $\text{Zn}_x\text{Fe}_{3-x}\text{O}_4$ mainly by WAXD techniques. The focus is concentrated on magnetization vs external magnetic field for a series of Zn-substituted ferrite ($\text{Zn}_x\text{Fe}_{3-x}\text{O}_4$) nanoparticles with different x . The analysis was pursued on two viewpoints. One is the crystal size estimated by using the modified Laue function as well as the crystal lattice spacing estimated by

Table 1. Values of M_s , H_c , and M_r for the Indicated x

	M_s (emu/g)	H_c (Oe)	M_r (emu/g)
$x = 0$	51.34	33.49	3.23
$x = 0.1$	73.54	17.22	1.32
$x = 0.2$	80.93	6.43	0.65
$x = 0.3$	77.71	10.57	1.15
$x = 0.4$	43.14	6.57	0.68

shifting of the center of gravity of the (311) plane. The other is the average magnetic moments estimated by the Brillouin function.

EXPERIMENTAL METHODS

Synthesis of Nanoparticles. Zinc-doped Fe_3O_4 particles represented as $\text{Zn}_x\text{Fe}_{3-x}\text{O}_4$ ($x = 0, 0.1, 0.2, 0.3, 0.4, 0.6, 1.0$) series were prepared by the coprecipitation method and by injecting a surface modifier simultaneously in one step. The x values were conventionally determined, based on the assumption that the amount of Zn doped into Fe_3O_4 is directly related to the molar ratios of Zn and Fe atoms in appropriate pure powders used for the following experiment. Three kinds of surface modifiers, 3-aminopropyltriethoxysilane (APTES), polyethylene glycol (PEG), and sodium dodecyl benzene sulfonate (SDBS), were used. Each modifier was added at the moment of magnetic crystal formation. Typically, appropriate pure powders of hexahydrated ferric chloride ($\text{FeCl}_3 \cdot 6\text{H}_2\text{O}$), tetrahydrated ferrous chloride ($\text{FeCl}_2 \cdot 4\text{H}_2\text{O}$), and zinc chloride (ZnCl_2) were dissolved in distilled water and thoroughly mixed for getting homogeneous solution under a nitrogen atmosphere to prevent Fe^{2+} from oxidation. Subsequently, the solution of modifier (APTES, PEG, or SDBS) in distilled water was added drop by drop into the chloride solution obtained in the last step with vigorous stirring (500 rpm) at 30 °C. After the above solution was mixed well, ammonium hydroxide (NH_4OH) was dripped into the intermixture to settle metal ions completely. A dark brown precipitation immediately appeared indicating the formation of $\text{Zn}_x\text{Fe}_{3-x}\text{O}_4$ magnetic particles. The suspension was stirred with constant velocity with maintaining ca. pH 10 for 1 h and then ripened for 3 h at 80 °C. The ripening process was of great benefit to prepare integrity crystal close to magnetism of inverse-spinel zinc ferrite. The black product was then subsided by applying a magnet and washed several times with distilled water until the pH value reached 7. The black product was washed with a large amount of ethanol 3 times subsequently. Then, the precipitate was dried in a vacuum oven at 60 °C for 24 h and grinded in a mortar.

Characterization. The structure of the samples was characterized with a D/max-2400 X-ray diffractometer (RIGAKU), using Cu K α radiation ($\lambda = 0.1542$ nm) with a step size of 0.02° in the 2θ ranging from 20° to 70° with divergent slit of 0.5 mm, operated at 40 kV and 150 mA. The intensity curves are obtained by some corrections like air scattering and polarization effect. The morphology and the distribution of the magnetic particles were also investigated, using a transmission electron microscope (TEM) (JEM-1010) at voltages of 100 kV. Magnetization was measured by a vibrating sample magnetometer (JDM-13) as a function of magnetic field up to 4400 Oe at 25 °C. Energy dispersion X-ray spectrometry (EDS) (Oxford Instruments X-Max) was used to analyze atomic elements of zinc-doped Fe_3O_4 particles under observation of scanning electron micrographs (SEM) at 20 kV.

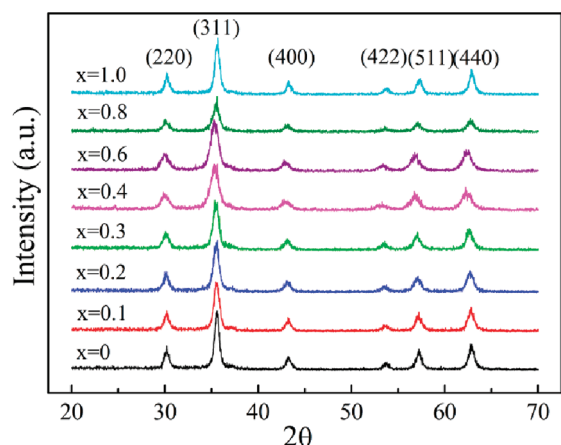


Figure 2. WAXD intensity distributions of $\text{Zn}_x\text{Fe}_{3-x}\text{O}_4$ ($x = 0, 0.1, 0.2, 0.3, 0.4, 0.6, 0.8, 1.0$).

Thermal gravimetric analysis (TGA) (TA-Q500) was used for weight loss measurements which were taken in the range from room temperature to 600 °C at a constant heating rate of 10 °C/min in nitrogen atmosphere. FTIR spectrometers (NEXUS) were recorded in KBr pellets in the range of 400–4000 cm^{-1} .

Incidentally, the magnetization and the crystal size of the resultant specimens were found to be independent of the surface modifiers, APTES, PEG, and SDBS. Hence the results obtained for SDBS were adopted in the present paper.

RESULTS AND DISCUSSION

Figure 1(a) shows magnetization curves measured at 25 °C by VSM for $\text{Zn}_x\text{Fe}_{3-x}\text{O}_4$ powders with different Zn^{2+} contents represented as $x = 0$ –0.4. The value of M_s beyond $x = 0.4$ is too small to be negligible. It is seen that the curves in the range of $x = 0$ –0.4 exhibited very small hysteresis, and they went through the origin reversibly. The values of residual magnetism (M_r) and coercivity (H_c) could be negligibly small compared with generated magnification (M) and applied magnetic field (H), respectively, for the specimens with $x = 0.1$ –0.4. These values are listed in Table 1. The magnification for all the zinc ferrite specimens increased linearly up to 500 Oe, and the magnification showed gradual increasing curve up to 2000 Oe. Beyond 2000 Oe, the magnification tended to level off, and they were all in saturated condition basically when the applied magnetic field reached 4400 Oe. Among the specimens, M_s was the highest at $x = 0.2$. The value of $\text{Zn}_{0.2}\text{Fe}_{2.8}\text{O}_4$ reached 80.93 emu/g. Judging from the M_s value and negligible hysteresis loop, it seems that the resultant $\text{Zn}_x\text{Fe}_{3-x}\text{O}_4$ are not ferromagnetism but superparamagnetism.^{2–4}

What should be particularly noted is that the M_s of $\text{Zn}_{0.2}\text{Fe}_{2.8}\text{O}_4$, 80.93 emu/g, has increased by 37.75% in comparison to that of pure Fe_3O_4 . This value is not only far higher than that of pure Fe_3O_4 but also the highest among most of the inverse-spinel ferrite materials doping with other metallic elements^{27–31} except Cu–Zn ferrites whose magnetization is beyond 100 emu/g but provides measurable hysteresis loop.¹⁷

Figure 1(b) shows the curves of $M/M(0)$ in the range of $H \geq 0$, which are normalized by M_s at 4400 Oe for $x = 0$. The curves reveal that M_s increases up to $x = 0.2$ and that the M_s at $x = 0.4$ is lower than that at $x = 0$. The curves shall be compared later with theoretical curves calculated by using the Brillouin function.

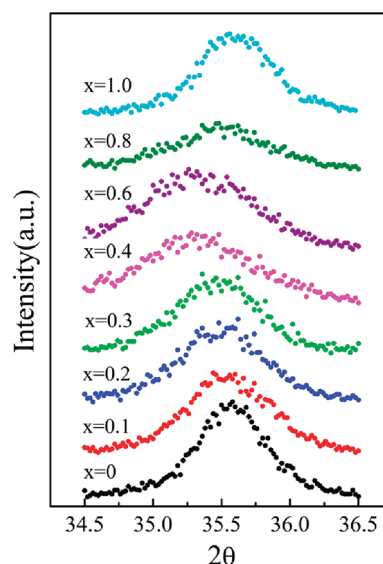


Figure 3. Enlargement of the diffraction intensity from the (311) plane.

A question can arise as to why M_s reached the maximum at $x = 0.2$ corresponding to a small amount of replacement of Fe^{3+} with Zn^{2+} in the A-site. This intriguing observation can be analyzed in terms of change in lattice spacing and crystallite size as well as in terms of superexchange interaction.

Figure 2 shows X-ray diffraction intensity distributions for Zn-doped Fe_3O_4 magnetic nanoparticles ($\text{Zn}_x\text{Fe}_{3-x}\text{O}_4$) with different Zn^{2+} contents ($x = 0$ –1). As can be seen in this figure, the diffraction peaks of $\text{Zn}_x\text{Fe}_{3-x}\text{O}_4$ are approximately similar to those of pure Fe_3O_4 ($x = 0$), indicating that all products have a crystal unit with face-centered cubic inverse-spinel structures.³⁹ The appearing peaks are contributed from the indexed crystal planes, (220), (311), (400), (422), (511), and (440), respectively.⁴⁰ To check the peak shift by changing x , the strongest diffraction peak from the (311) plane was chosen to investigate structural variation of the crystal unit.

Figure 3 shows the enlargement of the diffraction intensity from the (311) plane. The peak shift was estimated as that of the center of gravity of the diffraction curve as follows

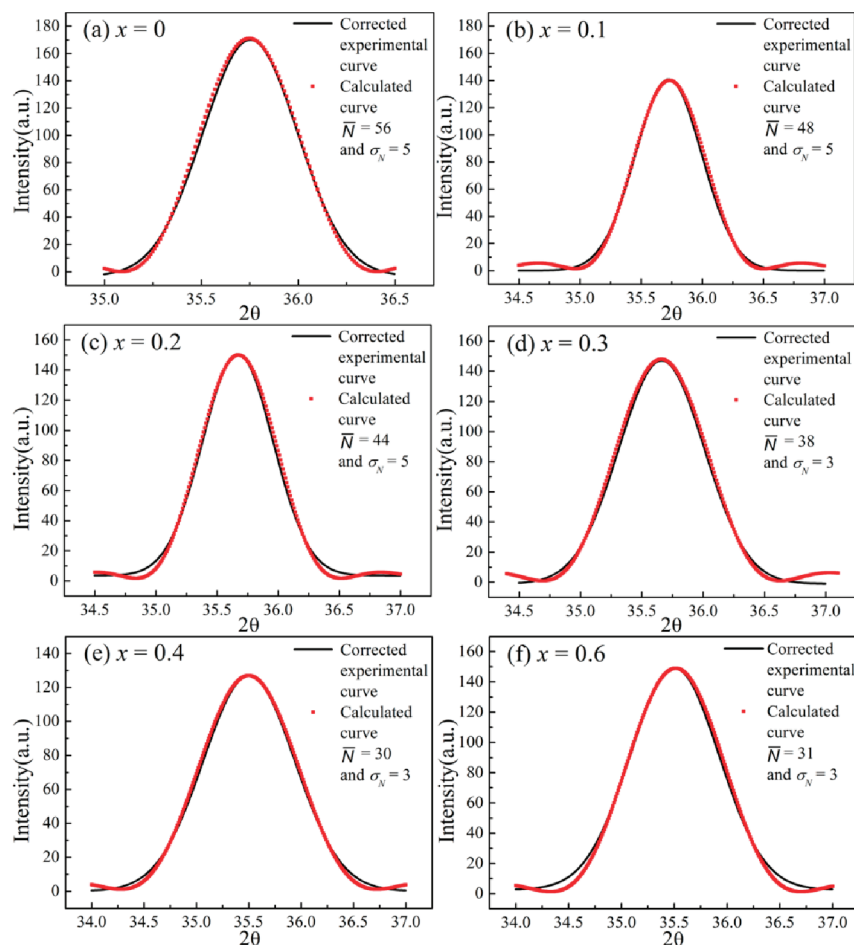
$$2\theta_{\text{max}} = \frac{\int_{2\theta_1}^{2\theta_2} 2\theta I(\theta) d\theta}{\int_{2\theta_1}^{2\theta_2} I(\theta) d\theta} \quad (1)$$

where $I(\theta)$ is the intensity distribution function curve and $2\theta_{\text{max}}$ is the corresponding average maxima concerning the diffraction peak position. In actual calculation, $2\theta_1$ and $2\theta_2$ are chosen as desirable values around 34.5 and 36.5, respectively. Each peak top evaluated by eq 1 is listed in Table 1.

As listed in Table 2, the peak top shifted toward lower angle with increasing x up to 0.4 and shifted inversely to higher angle beyond 0.4. This means that the lattice distance between the (311) planes varied by a transformation of the a -axis, which is listed in Table 2 together. The length of the a -axis became longer with increasing x up to 0.4, but further increase in x caused the decrease of the lattice distance. This means the replacement of Fe^{3+} with Zn^{2+} in the A site up to 0.4 caused the expansion of the crystal unit with the face-centered cubic inverse-spinel structure.

Table 2. Characteristics of the Crystal Domains for the Indicated x

label	β (deg)	$2\theta_{\max}$ ($^{\circ}$)	d (nm)	a (nm)	D_{311} (nm) (by Scherrer's eq)	\bar{N} (by eqs 2–5)	\bar{D} (nm) (by eqs 2–5)
$x = 0$	0.54	35.74	0.2512	0.8333	15.30	56	14.07
$x = 0.1$	0.63	35.73	0.2513	0.8335	12.99	48	12.06
$x = 0.2$	0.64	35.67	0.2517	0.8349	12.89	44	11.07
$x = 0.3$	0.65	35.65	0.2518	0.8353	12.70	38	9.56
$x = 0.4$	0.93	35.50	0.2529	0.8389	8.88	30	7.59
$x = 0.6$	0.88	35.52	0.2528	0.8384	9.43	31	7.84
$x = 0.8$	0.74	35.66	0.2518	0.8352	11.22	44	11.08
$x = 1.0$	0.57	35.79	0.2509	0.8321	14.43	54	13.55

Figure 4. Corrected experimental curves (solid curve) and calculated intensity distribution functions (dotted curves) for the indicated x .

To investigate the origin, detailed analysis of the X-ray diffraction intensity profile must be carried out in comparison between the experimental and theoretical diffraction intensity curves. In doing so, first of all, real experimental diffraction curves must be obtained. They could be obtained by convolution of two intensity distributions measured for silicon particles and each test specimen. Figure 4 shows the corrected real X-ray diffraction curves (solid curves) for the specimens, and the crystal sizes (D_{311}) calculated by Scherrer's equation are listed in Table 2, in which the constant value of K is set to be 0.89. Here it should be emphasized that Scherrer's equation can be formulated not only for perfect crystallites with no distance fluctuation between the crystal plane but also for a constant crystal size. If there are the

fluctuations for the distance and/or crystal size, the estimation by Scherrer's equation becomes meaningless. Hence theoretical calculation for a series of $\text{Zn}_x\text{Fe}_{3-x}\text{O}_4$ was carried out by taking into consideration for crystal size distribution.

Considering somewhat modification of Laue function, the diffraction intensity from perfect crystal with the crystal unit cell of N is given by

$$I(2\theta) = KC^2 \frac{\sin^2 \left[\frac{2\pi}{\lambda} Nd \sin \theta \right]}{\sin^2 \left[\frac{2\pi}{\lambda} d \sin \theta \right]} \quad (2)$$

where d is the lattice distance between the (311) planes listed in Table 2 and λ is the wavelength of X-ray given by 0.1542 nm. K and C are constant and structural factor, respectively. The detailed derivation is represented in the Appendix.

Here, it is plausible to consider that the number of crystal units has distribution. Since the crystal domain size of nanoparticles ($\text{Zn}_x\text{Fe}_{3-x}\text{O}_4$) is much smaller than the irradiated area by X-ray beam, there exist $\text{Zn}_x\text{Fe}_{3-x}\text{O}_4$ crystallites with several sizes in the irradiated area. In the present paper, the distribution of the number of crystal units proportional to crystal size distribution is given directly by Gaussian distribution as follows

$$PN = \frac{\exp\left\{-\frac{(N - \bar{N})^2}{2\sigma_N^2}\right\}}{\sum_{N=1}^{2\bar{N}-1} \exp\left\{-\frac{(N - \bar{N})^2}{2\sigma_N^2}\right\}} \quad (3)$$

where \bar{N} and σ_N are the average number of crystal units and its standard deviation, respectively.^{41,42} Hence the average diffraction intensity may be given by

$$\langle I(2\theta) \rangle = \sum_{N=1}^{2\bar{N}-1} P(N)I(2\theta) \quad (4)$$

The initial average number of \bar{N} to pursue computer simulation was conventionally estimated from the length of d and D_{311} listed in Table 2. The concept associated with eq 4 must be introduced to smear out the many subsidiary maxima on both sides of a main peak.^{41,42} To give the same height of peak tops between experimental and calculated curves, eq 4 is modified as follows

$$I_{\text{cal}}(\theta) = \frac{\langle I(2\theta) \rangle}{\langle I_{\text{top}}(2\theta) \rangle} I_{\text{exp}}(2\theta) \quad (5)$$

where $\langle I_{\text{top}}(2\theta) \rangle$ is the peak top intensity of the calculated intensity $\langle I(2\theta) \rangle$ and $I_{\text{exp}}(2\theta)$ is the peak top intensity of the corrected experimental intensity. Of course, $\langle I(2\theta) \rangle / \langle I_{\text{top}}(2\theta) \rangle$ becomes unity at twice the Bragg angle, providing the peak top of the calculated intensity.

As shown in Figure 4, the calculated intensity distribution functions (dotted curves) are in good agreement with the corrected experimental curves (solid curve) by selecting the average number \bar{N} of crystal units and the standard deviation σ_N . Of course, the values of \bar{N} and σ_N listed were obtained by curve fitting. The desirable average number \bar{N} of crystal units is slightly smaller than that obtained by Scherrer's equation directly. The value of σ_N is less sensitive to the curve profile in comparison with \bar{N} and is in the range from 3 to 5.

Figure 5(a) shows the distribution $P(N)$ of crystal unit number (upper side) and crystal size scale (lower side) at $x = 0$, 0.2, and 0.3. The size distribution D is given by $N \times d$. The average values of \bar{N} and \bar{D} ($= \bar{N} \times d$) corresponding to the peak top of $P(N)$ at each x (0–1) are listed together in Table 2. The value of \bar{N} becomes smaller with increasing x up to 0.4, indicating that zinc doping gives the damage for the Fe_3O_4 crystal. The size distribution in Figure 5(a) postulated by X-ray diffraction intensity curves supports the TEM micrographs in Figure 5(b) observed for the $\text{Zn}_{0.2}\text{Fe}_{2.8}\text{O}_4$ specimen with the highest M_s , which was coated with the surface modifier SDBS. Incidentally, the micrographs by addition of APTES and PEG were confirmed to be almost the same as the micrograph for SDBS in Figure 5(b).

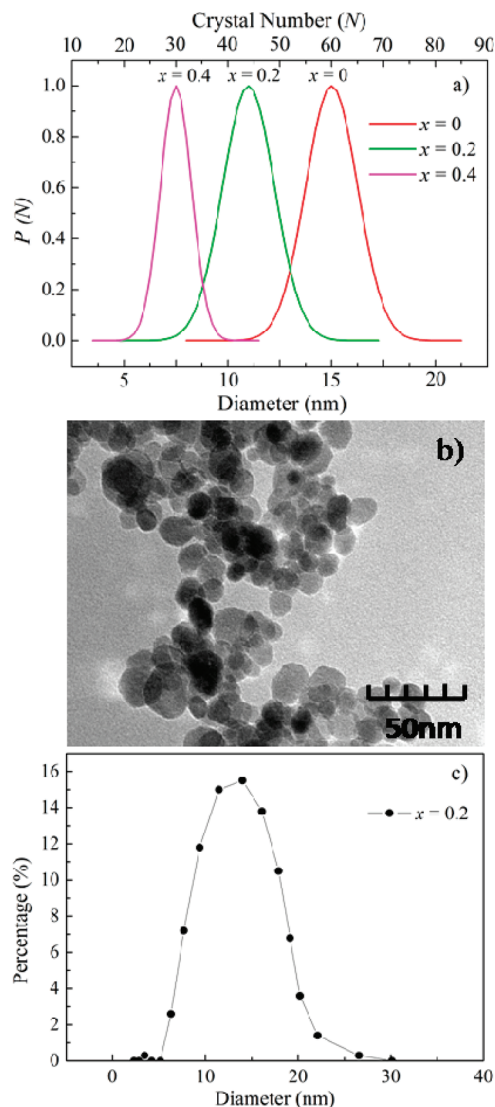


Figure 5. Distribution functions $P(N)$ of crystal unit number for the indicated x , which are calculated by using the values of \bar{N} and σ_N listed in each column.

No matter whether the modifiers were added, every particle showed a typical spherical shape which might be formed by the isotropic nucleation speed per unit area at the interface between $\text{Zn}_{0.2}\text{Fe}_{2.8}\text{O}_4$ domains,⁴³ but the dispersivity by the modifier became slightly better. Figure 5(c) shows domain size distribution estimated by TEM image, and the sizes are in the range of 10–15 nm. These sizes are in fairly good agreement with the average value of 11.1 nm (given by $\bar{D} = \bar{N} \times d$), estimated by X-ray. However, close observation reveals that the size by TEM is slightly bigger than that by X-ray diffraction. This indicates that each domain almost composed of a uniform crystal structure of $\text{Zn}_{0.2}\text{Fe}_{2.8}\text{O}_4$ and was not essentially agglomeration of the crystallites. That is, the size distribution for the spherical domain of $\text{Zn}_{0.2}\text{Fe}_{2.8}\text{O}_4$ by TEM image satisfies the theoretical calculation of the X-ray intensity curve in Figure 5(a). Judging from the average crystal size along the [311] direction estimated by X-ray diffraction technique and spherical crystal domain size observed by TEM, it is obviously reasonable to estimate size distribution statistically by using eq 5.

To pursue detailed discussion for the zinc doping effect, it should be repeated that the x value calculated from molar amounts of Zn^{2+} and Fe^{3+} atoms used in the experimental process is different from the x represented as $\text{Zn}_x\text{Fe}_{3-x}\text{O}_4$, especially when x is beyond 0.4. The derived two points are important: (1) the length of the a -axis became longer with increasing x up to 0.4, but beyond $x > 0.4$, it became shorter with increasing x up to unity. The length of the a -axis (0.8321 nm) at $x = 1$ is close to that (0.8333 nm) at $x = 0$. In contrast, the crystal unit number (crystal domain size) became smaller with increasing x up to 0.4, but it reversibly increased beyond 0.4.

The above two points suggest that zinc doping gives the damage for the Fe_3O_4 crystal. The $\text{Zn}_x\text{Fe}_{3-x}\text{O}_4$ crystal is less stable than the Fe_3O_4 one. As discussed before, $x = 0.4$ is thought to be an acceptable limit on forming the $\text{Zn}_x\text{Fe}_{3-x}\text{O}_4$ crystal since the radius (74 pm) of the Zn^{2+} ion incorporated in the A site is bigger than the radius (64 pm) of the replaced Fe^{3+} ion. The instinct for self-preservation for Fe^{3+} , Fe^{2+} , and O^{2-} ions becomes more prominent, when excess Zn^{2+} beyond 0.4 is dissolved in distilled water. At $x = 1$, such an instinct becomes most prominent, indicating that the replacement of Fe^{3+} with Zn^{2+} is hardly allowed under the crystal formation. Actually, the peak top of the X-ray diffraction peak tended to shift toward the top of Fe_3O_4 with increasing x beyond 0.6, and the peak top at $x = 1$ is close to the top of Fe_3O_4 . The same tendency is confirmed for the length of the a -axis. Obviously, the preparation possibility of ZnFe_2O_4 was almost zero at the present experiment since ZnFe_2O_4 was usually prepared by sintering at 600 °C,⁴⁴ and the a -axis of ZnFe_2O_4 must be longer than 0.8441 nm, different from the present value (0.8321 nm) at $x = 1$.

To investigate good dispersion of the particles by mixing, SDBS, TGA, and FTIR measurements were adopted, which are shown in Figure 6(a) and (b), respectively. Signals (1) and (2) in Figure 6 represent the results for uncoated and coated samples, respectively. The TGA and FTIR results indicated a certain amount of residual organic SDBS in the coated sample. In Figure 6(a), the weight loss of the coated sample was slightly distinguished in comparison with that of the uncoated sample, but the difference was very small because of many washings (more than 8 times) with distilled water and ethanol. The residual trace of SDBS was detected by FTIR spectra shown in Figure 6(b). The peaks at ~ 400 and $\sim 580\text{ cm}^{-1}$ were attributed to the stretching vibrations of Fe–O bonds in nanoparticles.⁴⁵ The existence of absorption bands at 880, 1050, and 2973 cm^{-1} , which correspond to the out-plane deformation vibrations of $=\text{C}-\text{H}$ bonds on the benzene ring, stretching vibrations of $\text{S}=\text{O}$ bonds, and stretching vibrations of $\text{C}-\text{H}$ bonds on the aliphatic chain, respectively, indicated the presence of SDBS on the surface of $\text{Zn}_{0.2}\text{Fe}_{2.8}\text{O}_4$ NPs even after several times (≥ 8) washing. The adsorbed water is featured by bands around 3420 and 1620 cm^{-1} , which are assigned to O–H stretching and H–O–H bending vibrations, respectively.

Judging from the results by Gnanaprakash et al.,⁴⁶ the functional groups of very small residual trace of SDBS bind to the surface of the particles, and the chains extend out into the nonpolar solvent, preventing aggregation of the particles by steric hindrance.

Figure 7 show EDS element spectra, and the spectra reveal that the peak of Zn becomes more intense in proportion to x . As an approximate evaluation, it is seen that the intensity ratio (Zn/Fe) estimated from the spectra is slightly higher than $x/(3-x)$ represented as the ratio for $\text{Zn}_x\text{Fe}_{3-x}\text{O}_4$.

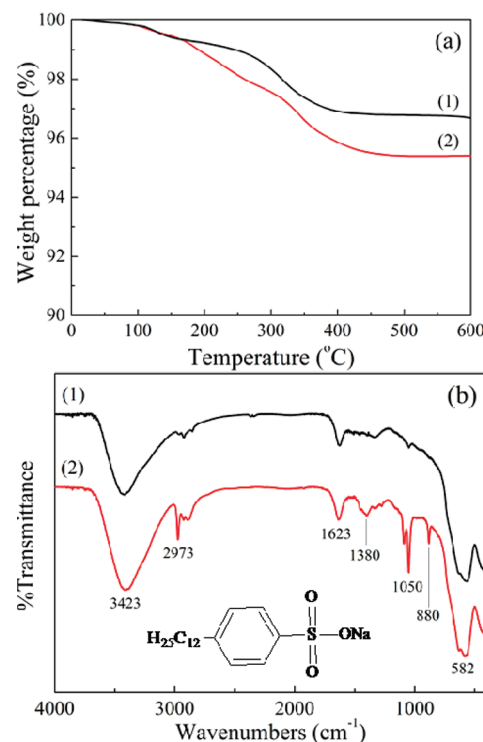


Figure 6. TGA curves (a) and FTIR spectrogram (b), in which (1) and (2) belong to uncoated and coated $\text{Zn}_{0.2}\text{Fe}_{2.8}\text{O}_4$ nanoparticles, respectively.

Judging from the chemical reaction described in Experimental Section, it may be expected that excess ZnCl_2 , which is independent of zinc doping of Fe_3O_4 , forms ZnO by chemical reaction with NH_4OH and/or remains as the hydrate on the surface of $\text{Zn}_x\text{Fe}_{3-x}\text{O}_4$ crystal domains without forming their crystal structures. Unfortunately, it was difficult to clean up excess Zn and Fe atoms without disrupting zinc-doped crystal domains. As shown in Figure 5(a) and (c), even at $x = 0.2$, the particle domain average size observed by TEM is slightly bigger than that estimated by X-ray diffraction. The small different sizes are probably thought to be due to tight adhesion of excess Zn and Fe compounds on the $\text{Zn}_{0.2}\text{Fe}_{2.8}\text{O}_4$ crystal domain surface. A series of experimental results provide that the magnetization for Zn-doped Fe_3O_4 against an applied magnetic field is extremely sensitive to Zn content as well as to crystal domain size.^{14–17}

As reported in a number of established papers, the number of Fe^{3+} ions in tetrahedral space (A-site), the Fe^{3+} ions being surrounded by four oxygen ions, is equal to that of in octahedral space (B-site), the Fe^{3+} or Fe^{2+} ions being surrounded by six oxygen atoms, and then the number of Fe^{3+} ions in the B-site is thought to be equal to that of Fe^{2+} ions in the B-site.^{37,47} In the B-site, however, the difference between Fe^{3+} and Fe^{2+} ions cannot be recognized, and the spin directions in Fe^{3+} and Fe^{2+} ions are the same, by double-exchange interaction leading to electron hopping between vicinal Fe^{3+} and Fe^{2+} ions through a hybrid orbital formed with the 2p orbital of an oxygen ion.

Recent studies of XPS spectra indicated a very small amount of Zn in the B-site.³³ To pursue theoretical calculation, however, the following discussion in this paper is based on the usual concept that the ion occupation in A- and B-sites is changed by zinc doping. The doping can replace Fe^{3+} ions with Zn^{2+} ions in the A-site, but no doping of Zn^{2+} occurs in the B-site.^{37,48}

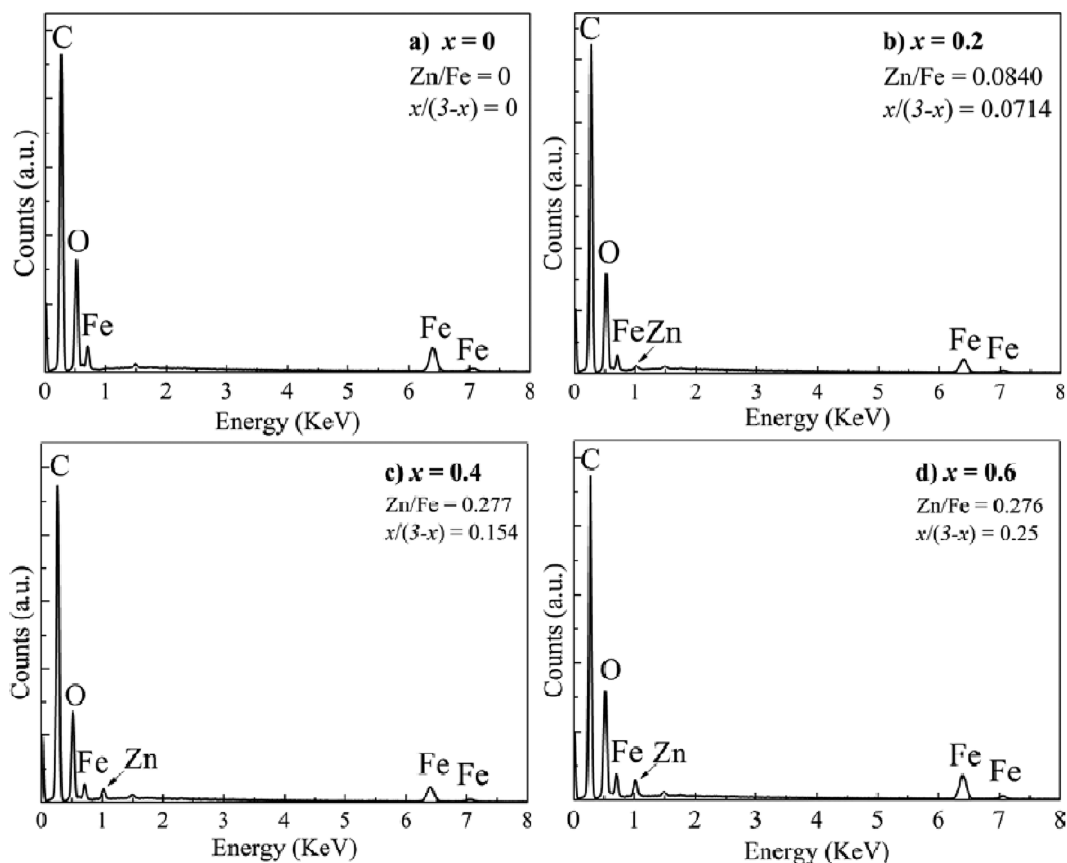


Figure 7. EDS spectra measured for zinc-doped ferric particles at the indicated molar ratio x , in which the peak of the C element belongs to the background independent of the zinc-doped Fe_3O_4 particles.

When Fe_x^{3+} ions in the A-site are replaced with Zn^{2+} ions, Fe^{2+} ions with the same number in the B-site change to Fe^{3+} by electron emission and form $[\text{Zn}_x^{2+}\text{Fe}_{1-x}^{3+}]_A[\text{Fe}_x^{3+}\text{Fe}_{1-x}^{2+}]_B\text{O}_4$. Judging from x -dependence on magnetization in Figure 1, the spin direction of the resultant Fe_x^{3+} ions in the B-site is thought to be sensitive to the x .

According to Hund's rule, Figure 8(a) shows a simplified example as a schematic diagram of replacement of Fe^{3+} with Zn^{2+} in the A-site. To facilitate understanding of the replacement, 10 Fe^{3+} ions in the A-site and 10 Fe^{3+} and 10 Fe^{2+} ions in the B-site are set at $x = 0$ (no zinc doping), and the disappearance of Fe^{3+} ions in the A-site with increasing x means the replacement with Zn^{2+} ions. In this case, the magnetic moment at $x = 0$ is offset perfectly by a superexchange transition between Fe^{3+} in the A-site and Fe^{3+} in the B-site, and the effective magnetic moment is only contributed from Fe^{2+} in the B-site. When one Fe_x^{3+} ion is replaced with a Zn^{2+} ion in the A-site ($x = 0.1$), one Fe^{2+} ion in the B-site changes to an Fe^{3+} ion with maintaining the same spin direction by one electron emission to preserve electric neutrality of the crystal unit. At $x = 0.2$, the similar electron transfer occurs for two Fe_x^{3+} ions. At $x = 0.3$, however, the spin directions of two Fe_x^{3+} ions among three Fe_x^{3+} ions are thought to be antiparallel to achieve the decrease of the magnetization, indicating generation of a superexchange interaction between the resultant Fe_x^{3+} and original Fe_x^{2+} ions through an oxygen ion in the B-site since some coupling angle of $\text{Fe}_x^{3+}-\text{O}-\text{Fe}^{2+}$ in the B-site becomes close to 180° . The superexchange interaction is thought to be predominant to the double-exchange one at x higher than 0.3. Hence at $x = 0.4$, the magnetization associated with four resultant

Fe_x^{3+} in the B-site becomes zero, and the total magnetization of Fe^{3+} in the B-site at $x = 0.4$ is equal to that at $x = 0$. If this is the case, the further zinc doping beyond 0.4 is thought to be meaningless. Actually, in the present experiment, M_s at $x = 0.5$ was very small to be negligible in comparison with that at $x = 0.4$.

On the basis of this assumption, numerical calculation for magnetization is carried out against an applied magnetic field. As for superparamagnetism of transition metal ions such as Fe^{3+} and Fe^{2+} , it has been reported that the number of effective Bohr magneton, n_{eff} , can be explained by using total spin number S rather than total angular momentum J represented as $J = L + S$, in which L is the angular momentum. The experimental values of n_{eff} are 5.9 and 5.2–5.5 for Fe^{3+} and Fe^{2+} , respectively. Both experimental values for Fe^{3+} and Fe^{2+} ions are similar to 5.92 and 4.90 calculated by using $2(S(S+1))^{1/2}$ rather than 5.92 and 6.71 calculated by using $g(J(J+1))^{1/2}$, respectively. As reported by an established textbook for magnetic properties, the angular quantum number L must be neglected. Hence J is mostly equal to the total spin number S of the d-orbital.

In accordance with quantum mechanics, the average magnetic moment $\langle \mu_J \rangle$ is given by Brillouin function as follows

$$\begin{aligned} \langle \mu_J \rangle &= Jg\mu_B \left[\frac{2J+1}{2J} \coth \left\{ \left(\frac{2J+1}{2J} \right) \frac{Jg\mu_B H}{kT} \right\} - \frac{1}{2J} \coth \left(\frac{Jg\mu_B H}{2JkT} \right) \right] \\ &= Jg\mu_B B_J \left(\frac{Jg\mu_B H}{kT} \right) \end{aligned} \quad (6)$$

where J is the total angular momentum; g is termed as the g -factor for spin given by 2.0023 assuming free electron; H is magnetic

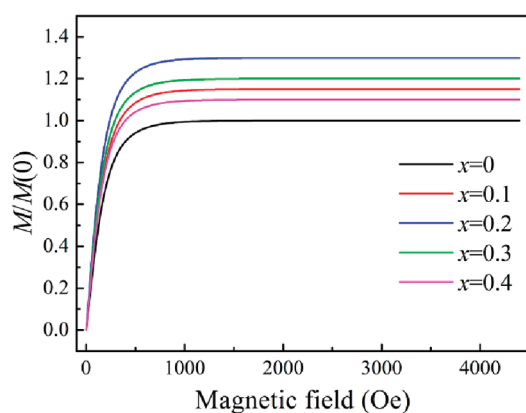
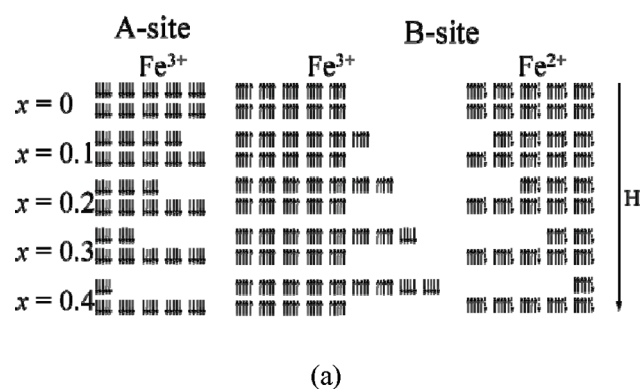


Figure 8. (a) Schematic diagram by replacement of Fe^{3+} ions with Zn^{2+} ions for $x = 0-0.4$ to represent superexchange interaction. The diagram is shown for 10 Fe^{2+} ions in the B-site, in which the spin for each ion is parallel or antiparallel with respect to the applied magnetic field H . (b) Calculated $M/M_s(0)$ based on model (a). $M_s(0)$ is the value at 4400 Oe for $x = 0$.

field; μ_B is Bohr magneton; k is Boltzmann constant; and T is absolute temperature. Because of no contribution from angular quantum number ($L = 0$), J for Fe^{2+} is given by $J_1 = 2$, while J for Fe^{3+} is given by $J_2 = 5/2$. Accordingly, the average magnetic moment of $\text{Zn}_x\text{Fe}_{3-x}\text{O}_4$ is represented as follows

$$\frac{\langle \bar{\mu}(x) \rangle}{2g\mu_B} = \frac{M(x)}{M_s(0)} = (1-x)\langle \mu_{J_1} \rangle + 0.4\langle \mu_{J_2} \rangle \quad x \leq 0.2 \quad (7)$$

and

$$\frac{\langle \bar{\mu}(x) \rangle}{2g\mu_B} = \frac{M(x)}{M_s(0)} = (1-x)\langle \mu_{J_1} \rangle + 2x\langle \mu_{J_2} \rangle \quad 0.2 < x \leq 0.4$$

Equation 7 is normalized by $M_s(0)$ (M_s at $x = 0$) to pursue the numerical calculation.

Figure 8(b) shows $M/M_s(0)$ curves calculated as a function of H at 25 °C. This figure can be compared with the experimental curves (see Figure 1(a)) normalized by $M_s(0)$ at 4400 Oe. As for the calculated curves for all the specimens, $M/M_s(0)$ represents a linear increase with increasing H and tends to level off beyond

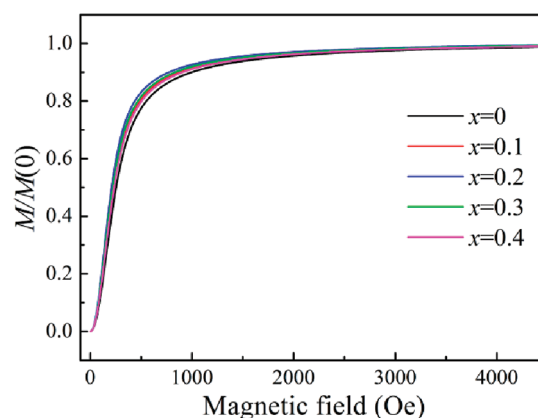
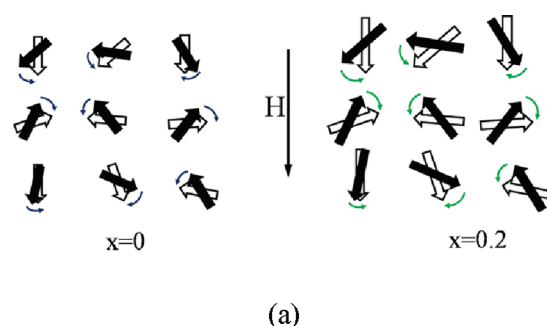


Figure 9. (a) Schematic diagram for the rotation of average magnetic moment with respect to the applied magnetic field H . (b) Calculated $M/M(0)$ based on model (a), in which the calculated curves are normalized by $M(0)$ at 4400 Oe for $x = 0$.

$H = 500$ (Oe). The value saturates perfectly beyond 1500 Oe. The saturated magnetization (M_s) increases with increasing x , and M_s becomes highest at $x = 0.2$. The value of M_s at $x = 0.3$ is higher than that at $x = 0.1$. This tendency is in good agreement with the normalized experimental curves in Figure 1 (b). In Figure 8(b), the calculated value of M_s at $x = 0.4$ is higher than that at $x = 0$, while in Figure 1(b) the normalized experimental value of M_s at $x = 0.4$ is much lower than that at $x = 0$. Such a discrepancy for calculated and experimental $M/M_s(0)$ is probably due to the fact that the calculation was carried out by using eq 6 formulated without taking into consideration the crystal size distribution by zinc doping size.

As listed in Table 2, the crystal size becomes smaller with increasing x up to 0.4. The radius of the Zn^{2+} ion is 74 pm, which is bigger than that of Fe^{3+} (64 pm). Hence, the zinc doping seems to cause expansion of the a -axis indicating considerable instability of the crystal unit. The numerical calculation shown in Figure 5(a) reveals that the average number of crystal units decreases with increasing x . Actually, the experimental M_s tends to decrease beyond $x = 0.2$, and M against H could not be measured at $x = 0.5$ indicating the impossibility of further zinc doping.

The further discrepancy for calculated and experimental $M/M_s(0)$ is saturation of M against H . As discussed already, all the calculated $M/M_s(0)$ are in saturated condition at 1000 Oe, while all the experimental $M/M_s(0)$ in Figure 1(b) tend to increase beyond 1000 Oe. There are two improvable possibilities to solve the discrepancy. One is change on crystal size distribution

due to Zn doped into Fe_3O_4 , as discussed before, and the other is the magnetic moment angle of particle domains with respect to the applied magnetic field (H) direction. Mathematical treatment for the former case is very complicated, and the latter case is discussed in the present paper.

The model in Figure 8(a) is constructed in the case where the magnetic moment of $[\text{Zn}_x^{2+}\text{Fe}_x^{3+}]_A[\text{Fe}^{3+}\text{Fe}_x^{3+}\text{Fe}_{1-x}^{2+}]_B\text{O}_4$ is parallel to the applied magnetic field H . To moderate the rapid saturation, another model is proposed. That is, the total magnetic field of each element is assumed to be oriented at polar angle θ with respect to the applied magnetic field as shown in Figure 9(a), in which the average magnetic moment as a vector at $x = 0.2$ is represented longer than that at $x = 0$. In this case, the average magnetic moment along H is given by

$$\frac{\langle \bar{\mu}(\cos \theta) \rangle}{\langle \bar{\mu}(x) \rangle} = \frac{\int_{-1}^1 \cos \theta \exp \left\{ \frac{\langle \bar{\mu}(x) \rangle H \cos \theta}{kT} \right\} d(\cos \theta)}{\int_{-1}^1 \exp \left\{ \frac{\langle \bar{\mu}(x) \rangle H \cos \theta}{kT} \right\} d(\cos \theta)} \quad (8)$$

The numerical calculation of eq 8 was done by normalizing by $\langle \mu(0) \rangle$ at $H = 10\,000$ Oe. Figure 9(b) shows the calculated curves. The saturation of the calculated curves becomes slowly advancing rather than that shown in Figure 8(b). However, the difference of M_s by varying x becomes less effective, and M_s tends to unity. The orientation effect of the magnetic moment could not dissolve the rapid saturation of M .

Accordingly, a series of experiments may lead to such conclusions that an increase of magnetization by the amount of Zn doped into Fe_3O_4 is sensitive to the number of resultant doped crystal units as well as expansion of the crystal lattice, and then excess zinc doing causes disruption of the original Fe_3O_4 crystal. Further improvement must be taken into consideration as a future subject.

Of course, there are reports that M_s reached the maximum at $x = 0.3$.³³ If this is the case, the spin direction of the resultant Fe^{3+} ions in the B-site must be the same, and the M_s at $x = 0.4$ must be close to that at $x = 0.2$. Such a mode is quite different from the present experimental results in Figure 1. Accordingly, the model in Figure 8(a) is adopted in the present case. However, the maximum of M_s at $x = 0.3$ must be kept as one of the possibilities due to variation character of sample preparations.

CONCLUSION

Zn-doped Fe_3O_4 nanoparticles with excellent superparamagnetism and high saturated magnetization have been successfully prepared by the chemical coprecipitated method in the presence of a surface modifier. The superparamagnetic properties of the zinc ferrite samples were confirmed by such a magnetization behavior against external magnetic field that all the hysteresis loops went through the origin reversibly without residual magnetism and coercivity. With an increase in zinc content, the saturation magnetization of $\text{Zn}_x\text{Fe}_{3-x}\text{O}_4$ particles offered up-grade first and then tended to fall off. The magnetic mechanism was elucidated by replacement of Fe^{2+} ions with Fe^{3+} ions in the B-site by one-electron emission in each Fe^{2+} ion. The average magnetic moment calculated at the $x = 0, 0.1, 0.2, 0.3$, and 0.4 demonstrated that the saturated value reached the maximum at

$x = 0.2$. The corresponding X-ray diffraction curves revealed that the decrease of crystal size was confirmed by zinc doping, and this tendency became considerable with increasing x . To study such phenomena, detailed analysis for the X-ray diffraction intensity curve was analyzed in terms of the curve profile and the peak top shift by using modified Laue function. It turned out that the further increase in zinc doping beyond $x = 0.2$ caused the decrease of the number of the face-centered cubic units with inverse-spinel structure as well as the expansion of the a -axis leading to disruption of the Fe_3O_4 crystal, and the analysis was supported by TEM observation.

APPENDIX

In the geometrical arrangement to detect an X-ray diffraction beam in the horizontal direction, the reciprocal lattice vector of the n_r -th crystal plane located at \mathbf{r} from a center of crystal system may be given by

$$\mathbf{r} = \left\{ \sin \left(\frac{\pi}{2} + \theta \right) \mathbf{j} + \sin \left(\frac{\pi}{2} + \theta \right) \mathbf{i} \right\} d = (\mathbf{j} \cos \theta - \mathbf{i} \sin \theta) n_r d$$

The scattering unit vector \mathbf{s} is defined by $(\mathbf{s}_0 - \mathbf{s}')$ where \mathbf{s}_0 and \mathbf{s}' are the vectors of incident and scattering beams, which is given by

$$\mathbf{s} = \mathbf{i}(1 - \cos 2\theta) - \mathbf{j} \sin 2\theta = 2 \sin \theta (\mathbf{i} \sin \theta - \mathbf{j} \cos \theta)$$

Hence we have

$$(\mathbf{r} \cdot \mathbf{s}) = -2d \sin \theta$$

In the present system, the Laue function for total crystal number N , which is proportional to the scattering amplitude E , may be rewritten as follows

$$\begin{aligned} E &\propto \sum_{n_i=0}^{N-1} \exp \left[\frac{2\pi i}{\lambda} n_i \left(\frac{\mathbf{a}}{h} + \frac{\mathbf{a}}{k} + \frac{\mathbf{a}}{l} \right) \cdot \mathbf{s} \right] \\ &= \sum_{n_i=0}^{N-1} \exp \left[\frac{2\pi i}{\lambda} n_i (\mathbf{r} \cdot \mathbf{s}) \right] = \sum_{n_i=0}^{N-1} \exp \left[\frac{4\pi i}{\lambda} n_i d \sin \theta \right] \\ &= \frac{1 - \exp \left[\frac{4\pi i}{\lambda} N d \sin \theta \right]}{1 - \exp \left[\frac{4\pi i}{\lambda} d \sin \theta \right]} = \frac{\exp \left[\frac{2\pi i N d}{\lambda} \sin \theta \right] \sin \left[\frac{2\pi N d}{\lambda} \sin \theta \right]}{\exp \left[\frac{2\pi i d}{\lambda} \sin \theta \right] \sin \left[\frac{2\pi d}{\lambda} \sin \theta \right]} \end{aligned}$$

When the crystal is set on the center of the coordinate, the exponential terms of numerator and denominator disappear. The diffraction intensity is given by

$$I = KC^2EE^* = KC^2 \frac{\sin^2 \left(\frac{2\pi N d}{\lambda} \sin \theta \right)}{\sin^2 \left(\frac{2\pi d}{\lambda} \sin \theta \right)}$$

where C is the structural factor and K is a constant.

AUTHOR INFORMATION

Corresponding Author

*E-mail: mm-matsuo@live.jp.

ACKNOWLEDGMENT

This work was supported by the National Natural Science Foundation of China (NSFC) program (No. 21074016).

The authors acknowledge Dr. Taiyo Yoshioka, Toyota Technological Institute, for his great assistance in TEM experiments.

REFERENCES

- (1) Laurent, S.; Forge, D.; Port, M.; Roch, A.; Robic, C.; Vander Elst, L.; Muller, R. N. *Chem. Rev.* **2008**, *108*, 2064–2110.
- (2) Jeong, U.; Teng, X.; Wang, Y.; Yang, H.; Xia, Y. *Adv. Mater.* **2007**, *19*, 33–60.
- (3) Roca, A. G.; Marco, J. F.; Morales, M. d. P.; Serna, C. J. *J. Phys. Chem. C* **2007**, *111*, 18577–18584.
- (4) Leslie-Pelecky, D. L.; Rieke, R. D. *Chem. Mater.* **1996**, *8*, 1770–1783.
- (5) Meng, J.; Yang, G.; Yan, L.; Wang, X. *Dyes Pigm.* **2005**, *66*, 109–113.
- (6) Cha, H. G.; Kim, C. W.; Kang, S. W.; Kim, B. K.; Kang, Y. S. *J. Phys. Chem. C* **2010**, *114*, 9802–9807.
- (7) Hu, A.; Yee, G. T.; Lin, W. J. *Am. Chem. Soc.* **2005**, *127*, 12486–12487.
- (8) Li, X.; Zhang, B.; Ju, C.; Han, X.; Du, Y.; Xu, P. *J. Phys. Chem. C* **2011**, *115*, 12350–12357.
- (9) Cui, Z. M.; Jiang, L. Y.; Song, W. G.; Guo, Y. G. *Chem. Mater.* **2009**, *21*, 1162–1166.
- (10) Casula, M. F.; Floris, P.; Innocenti, C.; Lascialfari, A.; Marinone, M.; Corti, M.; Sperling, R. A.; Parak, W. J.; Sangregorio, C. *Chem. Mater.* **2010**, *22*, 1739–1748.
- (11) Sen, T.; Sebastianelli, A.; Bruce, I. J. *Am. Chem. Soc.* **2006**, *128*, 7130–7131.
- (12) Sun, C.; Lee, J. S. H.; Zhang, M. *Adv. Drug Delivery Rev.* **2008**, *60*, 1252–1265.
- (13) Gupta, A. K.; Gupta, M. *Biomaterials* **2005**, *26*, 3995–4021.
- (14) Xuan, S.; Wang, Y. X. J.; Yu, J. C.; Cham Fai Leung, K. *Chem. Mater.* **2009**, *21*, 5079–5087.
- (15) Kittel, C. *Phys. Rev.* **1946**, *70*, 965–971.
- (16) Song, Q.; Zhang, Z. J. *J. Phys. Chem. B* **2006**, *110*, 11205–11209.
- (17) Pu, Y.; Tao, X.; Zeng, X.; Le, Y.; Chen, J.-F. *J. Magn. Magn. Mater.* **2010**, *322*, 1985–1990.
- (18) Li, J.; Huang, Z.; Wu, D.; Yin, G.; Liao, X.; Gu, J.; Han, D. *J. Phys. Chem. C* **2010**, *114*, 1586–1592.
- (19) Kakol, Z.; Honig, J. M. *Phys. Rev. B* **1989**, *40*, 9090–9097.
- (20) Goya, G. F.; Rechenberg, H. R. *J. Magn. Magn. Mater.* **1999**, *203*, 141–142.
- (21) Teja, A. S.; Koh, P.-Y. *Prog. Cryst. Growth Charact. Mater.* **2009**, *55*, 22–45.
- (22) Kang, Y. S.; Risbud, S.; Rabolt, J. F.; Stroeve, P. *Chem. Mater.* **1996**, *8*, 2209–2211.
- (23) Capek, I. *Adv. Colloid Interface Sci.* **2004**, *110*, 49–74.
- (24) Tang, N. J.; Zhong, W.; Jiang, H. Y.; Wu, X. L.; Liu, W.; Du, Y. W. *J. Magn. Magn. Mater.* **2004**, *282*, 92–95.
- (25) Sun, X.; Zheng, C.; Zhang, F.; Yang, Y.; Wu, G.; Yu, A.; Guan, N. *J. Phys. Chem. C* **2009**, *113*, 16002–16008.
- (26) Wang, H.; Hu, P.; Pan, D. a.; Tian, J.; Zhang, S.; Volinsky, A. A. *J. Alloys Compd.* **2010**, *502*, 338–340.
- (27) Yao, C.; Zeng, Q.; Goya, G. F.; Torres, T.; Liu, J.; Wu, H.; Ge, M.; Zeng, Y.; Wang, Y.; Jiang, J. Z. *J. Phys. Chem. C* **2007**, *111*, 12274–12278.
- (28) Jacintho, G. V. M.; Brolo, A. G.; Corio, P.; Suarez, P. A. Z.; Rubim, J. C. *J. Phys. Chem. C* **2009**, *113*, 7684–7691.
- (29) He, Q.; Wang, H. Z.; Wen, G. H.; Sun, Y.; Yao, B. *J. Alloys Compd.* **2009**, *486*, 246–249.
- (30) Li, L.; Li, G.; Smith, R. L.; Inomata, H. *Chem. Mater.* **2000**, *12*, 3705–3714.
- (31) Mozaffari, M.; Manouchehri, S.; Yousefi, M. H.; Amighian, J. *J. Magn. Magn. Mater.* **2010**, *322*, 383–388.
- (32) Gupta, R.; Sood, A. K.; Metcalf, P.; Honig, J. M. *Phys. Rev. B* **2002**, *65*, 104430.
- (33) Wen, M.; Li, Q.; Li, Y. *J. Electron Spectrosc. Relat. Phenom.* **2006**, *153*, 65–70.
- (34) Srivastava, C. M.; Shringi, S. N.; Srivastava, R. G.; Nanadikar, N. G. *Phys. Rev. B* **1976**, *14*, 2032.
- (35) Srivastava, C. M.; Shringi, S. N.; Srivastava, R. G. *Phys. Rev. B* **1976**, *14*, 2041.
- (36) Lu, Z. L.; Lv, L. Y.; Zhu, J. M.; Li, S. D.; Liu, X. C.; Zou, W. Q.; Zhang, F. M.; Du, Y. W. *Solid State Commun.* **2006**, *137*, 528–532.
- (37) Verwey, E. J. W.; Heilmann, E. L. *J. Chem. Phys.* **1947**, *15*, 174–180.
- (38) Shim, J. H.; Lee, S.; Min, B. I. *Phys. Rev. B* **2007**, *75*, 134406–1–134406–5.
- (39) Tan, Y.; Zhuang, Z.; Peng, Q.; Li, Y. *Chem. Mater.* **2008**, *20*, 5029–5034.
- (40) Abareshi, M.; Goharshadi, E. K.; Mojtaba Zebarjad, S.; Khandan Fadafan, H.; Youssefi, A. J. *Magn. Magn. Mater.* **2010**, *322*, 3895–3901.
- (41) Bin, Y.; Oishi, K.; Koganemaru, A.; Zhu, D.; Matsuo, M. *Carbon* **2005**, *43*, 1617–1627.
- (42) Matsuo, M.; Sawatari, C.; Tsuji, M.; Manley, R. S. J. *J. Chem. Soc., Faraday Trans.* **1983**, *79*, 1593–1605.
- (43) Kim, D. K.; Mikhaylova, M.; Zhang, Y.; Muhammed, M. *Chem. Mater.* **2003**, *15*, 1617–1627.
- (44) Chia, C. H.; Zakaria, S.; Yusoff, M.; Goh, S. C.; Haw, C. Y.; Ahmadi, S.; Huang, N. M.; Lim, H. N. *Ceram. Int.* **2010**, *36*, 605–609.
- (45) Waldron, R. D. *Phys. Rev.* **1955**, *99*, 1727–1735.
- (46) Gnanaprakash, G.; Philip, J.; Jayakumar, T.; Raj, B. *J. Phys. Chem. B* **2007**, *111*, 7978–7986.
- (47) Shinagawa, T.; Izaki, M.; Inui, H.; Murase, K.; Awakura, Y. *Chem. Mater.* **2006**, *18*, 763–770.
- (48) Grasset, F.; Labhsetwar, N.; Li, D.; Park, D. C.; Saito, N.; Haneda, H.; Cador, O.; Roisnel, T.; Mornet, S.; Duguet, E.; Portier, J.; Etourneau, J. *Langmuir* **2002**, *18*, 8209–8216.